https://dx.doi.org/10.1016/j.ijheatmasstransfer.2020.120629

Mathematical modeling of direct formate fuel cells incorporating the effect of ion migration

Xiangyu Su[#,1], Zhefei Pan[#,1], Liang An*[,1], Yaoguang Yu*[,2]

[1]Department of Mechanical Engineering, The Hong Kong Polytechnic University, Hung Hom, Kowloon, Hong Kong SAR, China.

[2]School of Materials, Sun Yat-sen University, Shenzhen 518107, China

[#]Equal contribution.

*Corresponding authors.

Email: liang.an@polyu.edu.hk (L. An)

Email: yuyg5@mail.sysu.edu.cn (Y.G. Yu)

Abstract

In this work, a one-dimensional mathematical model of direct formate fuel cells is developed. The present model involves mass/charge transport and electrochemical reactions. Compared to the previous models, this model incorporates the ion migration and considers the anode catalyst layer thickness, so that this model is not only capable of predicting the polarization curves to evaluate the fuel cell performance, but also able to give more in-depth insights into the direct formate fuel cells, e.g., the concentration distributions of the reactants/products, the local current density distributions, and the distribution of electrode potential. In validation, the present model results agree well with the experimental data from the open literature. The voltage losses resulting from the anode, membrane and cathode, as well as the distribution of the electrode potential are specified individually via using the present model. Moreover, the effects of the operating conditions,

i.e., the feeding concentrations of reactants, and the structural design parameters, i.e., the thicknesses and porosities of diffusion layers and catalyst layers as well as the specific active surface area of the catalyst layers, on the fuel cell performance are examined.

Keywords: Fuel cells; Direct formate fuel cells; Mathematical modeling; Ion migration; Catalyst layer; Potential distribution

1. Introduction

Direct formate fuel cells (DFFCs) can directly convert the chemical energy stored in formate into electricity [1], which possess various advantageous characteristics: i) formate, referring to sodium formate (HCOONa) and potassium formate (HCOOK) salts, is solid, inflammable, non-toxic, thereby, it is easy to store, transport and handle, which provides much more economic and convenient fuel operation as compared to hydrogen and other liquid fuels [2-13]; ii) formate oxidation reaction (FOR) is facile in the alkaline medium [1, 14]; iii) the theoretical voltage of DFFCs is as high as 1.45 V, which is 0.24 V higher than direct methanol fuel cells [15], 0.31 V higher than direct ethanol fuel cells [16] and 0.46 V higher than direct ethylene glycol fuel cells [6]; iv) formate can serve as the energy storage medium for various alternative energy technologies, e.g., solar, wind, geothermal, wave, and nuclear power, since they can be produced from electrochemical or photoelectrochemical reactions [17]; and v) superior to other direct liquid fuels that possess incomplete oxidation products, formate is completely oxidized into water and carbon dioxide, resulting in a high electron transfer rate of 100%. For those reasons, extensive experimental investigations have been conducted to upgrade their performance [18-28]. Bartrom et al. [18] demonstrated the first anion exchange membrane (AEM) DFFC. This fuel cell resulted in a peak power density (PPD) of 144 mW cm^{-2} at 60 ^{o}C. After that, Bartrom et al. [19] optimized the anode preparation method and further increased the PPD to 267 mW cm^{-2} under the same operating conditions. Nguyen et al. [20], Jiang et al. [21], Wang et al. [22] and Miller et al. [23] studied the Pt-free DFFCs. Nguyen et al. [24] adopted the optimized anode proposed by Bartrom et al. [19] in an AEM DFFC. This DFFC achieved a PPD of 64 mW cm^{-2} and 106 mW cm^{-2} at 23 ^{o}C and 50 ^{o}C, respectively. Sun et

al. [25] investigated the effect of the usage of quaternary ammonia polysulfone anion-ionomer in electrodes on the performance of DFFCs. It was found that the anion-ionomer-free DFFC yielded a PPD of 41 mW cm^{-2} at 40 ºC. The performance was 40% higher than that of the DFFC using the quaternary ammonia polysulfone anion-ionomer-based electrodes. Su et al. [26] proposed and fabricated a passive DFFC. This passive DFFC achieved a peak power density of 16.6 mW cm^{-2} without using any auxiliary devices such as pumps, gas compressors, and gas blowers. Su et al. [27] further improved the DFFC performance by employing innovative three-dimensional porous electrode design. They proposed and fabricated a Pd/C nanoparticles coating on the nickel foam matrix surface (Pd-C/NF) via a dip-coating method, and with this electrode as anode, a peak power density of 45.0 mW cm^{-2} at 60 ºC, which is two times of that achieved by using a conventional dual-layer design (19.5 mW cm^{-2}). Li et al. [28] proposed and demonstrated a cation exchange membrane based DFFC, which can produce electricity (PPD: 20.0 mW cm^{-2}) and NaOH. Therefore, it can be seen that a significant progress has been achieved by the previous experimental investigations.

Mathematical models are effective and important tools in fuel cell research. They can serve several important functions: i) to predict the fuel cell performance and evaluate structural and operating parameters, ii) to give the insights of the local message in fuel cells, and iii) to investigate and examine how the operating conditions and structural design parameters affect the fuel cell performance. In the past decades, many mathematical models have been developed for alkaline fuel cells [29-34]. Jiao et al. [29] developed a one-dimensional analytical model for alkaline AEM hydrogen fuel cells. The model took into consideration of the gas transport, electrochemical reactions and water crossover driven by electro-

osmotic force. Based on this model, it was found that the cathode humidification had a dominant effect on the performance of an AEM hydrogen fuel cell and explained that why the water in the cathode was consumed much faster than oxygen is because of the cathodic reaction and the electro-osmotic drag when using AEM as the polymer electrolyte. Deng et al. [30] developed a one-dimensional analytical model for alkaline AEM direct methanol fuel cells. It was found that the feeding concentration of methanol, the operating temperature and the membrane thickness were three key factors affecting the fuel cell performance, as compared to the other parameters, i.e., flow rate, the humidification of the fed oxygen/air, the porosities of the anode diffusion layer/anode catalyst layer and the cell orientation. Heysiattalab et al. [31] proposed and developed a two-dimensional analytical model for direct ethanol fuel cells. The model considered the transport of the reactants in the anode and cathode, as well as the ethanol crossover through the membrane. Based on the model, it was found that the ethanol concentration varied almost linearly in the anode channel, and the cathode overpotential remained almost zero while the anode overpotential would increase with the current density. Pan et al. [32] proposed and developed a one-dimensional analytical model for alkaline-acid direct ethylene glycol fuel cells, which included the effects of the competitive adsorption and the ethylene glycol crossover. The effects of the operating conditions and the electrode design parameters on the fuel cell performance was comprehensively examined. Mathematical model has also been used in DFFCs. An et al. [33] developed a one-dimensional analytical model considering the transport mechanism of diffusion and the electrochemical reactions. In addition, the effects of the structural design parameters and the operating conditions were investigated as well. Not only the cell performance but also the local reactant concentrations and the electrode

overpotentials were specified based on this model. Moreover, the catalyst layer was simplified as an interface, and thus the electrode potential distribution cannot be specified. Su et al. [34] investigated the ion transport characteristics through different types of ion exchange membrane in DFFCs using a one-dimensional model. The modeling results show that, when using an AEM, both formate and hydroxide concentrations in the anode catalyst layer are higher than those achieved by using a cation exchange membrane. Although a thicker membrane better alleviates the fuel crossover phenomenon, increasing the membrane thickness will increase the ohmic loss, due to the larger ion-transport distance through the membrane.

The previous models about fuel cells adopted the simplification that the mass/charge transport of the reactants in the solution electrolyte is diffusion-predominated. In alkaline fuel cells, however, the reactants include the negatively charged OH^- ions, in addition to various molecules. In DFFCs, the aqueous fuel solution also contains metal cations, e.g., Na^+ or K^+, and anions, e.g., OH^-, CO_3^{2-} and $HCOO^-$. The transport of cations and anions is not only driven by the concentration gradient, but also influenced by the potential difference in the porous electrode saturated with liquid electrolyte. Hence, the transport mechanism of ion migration has to be considered for more accurate predictions. In addition, considering the migration of the charged ions can reveal the local current density distributions. Motivated by the need and benefit, in this work, a one-dimensional model for AEM DFFCs is developed. The various physical and chemical processes in a DFFC are considered: i) the diffusion and migration of reactants/products in porous anode diffusion layer and catalyst layer, ii) a reactant concentration-dependent anodic kinetics in the anode catalyst layer, and iii) ionic current conduction across AEM. The validations show that the

modeling result well agrees with the experimental data [18]. The voltage losses of the anode, membrane and cathode, as well as the distribution of the electrode potential, can be specified. Furthermore, the effects of the operating and structural design parameters on the fuel cell performance are investigated and analyzed.

2. Model formulation

2.1. Computational domain and chemical & physical processes

A typical AEM DFFC is constructed in a layer-by-layer configuration, which can be divided into seven domains, as shown in Figure 1: i) anode flow field (AFF), ii) anode diffusion layer (ADL), iii) anode catalyst layer (ACL), iv) AEM, v) cathode catalyst layer (CCL), vi) cathode diffusion layer (CDL) and vii) cathode flow field (CFF).

During the operation of the DFFC, the fuel solution, which is containing HCOOK and KOH, and the oxygen are supplied into the AFF and CFF, respectively. The fuel solution flowing through the AFF delivers the reactants to the ACL. In the ACL, the reactants participate in the FOR on the active surface of the anode:

$$HCOO^- + 3OH^- \rightarrow CO_3^{2-} + 2H_2O + 2e^- \qquad E^0_{FOR} = -1.05\ V \qquad (1)$$

The consumption of reactants as a result of the FOR creates concentration gradients of each species, which causes the transport of the reactants from the AFF to the ACL and the transport of the products in the opposite direction. The transport of the charged ions is further subjected to the electrolyte potential difference, causing the migration of charged ions.

The electrons released from the anodic reaction transport to the cathode via the external circuit, driven by the electric potential difference between two electrodes. A part of the anode solution crosses the membrane to the cathode, due to the existence of pressure and concentration differences between the two sides. In the CCL, the delivered electrons, crossovered water and fed oxygen participate in the ORR on the active surface of the CCL to generate OH^- ions:

$$H_2O+\frac{1}{2}O_2+2e^-\rightarrow 2OH^- \qquad E^0_{ORR} = 0.40\ V \qquad (2)$$

The consumption of O_2 in the CCL leads to the delivery of O_2 from the CFF towards the CCL. The produced OH^- ions transport through the membrane to the anode driven by electrolyte potential difference, completing the ionic circuit.

In summary, the operation of an AEM DFFC fueled with HCOOK, involves four main physical and chemical processes: i) the transport of various species, i.e., K^+, $HCOO^-$, OH^-, CO_3^{2-} and O_2, ii) the electrochemical reactions on the active surface, iii) the ionic current through the membrane, and iv) the electronic and ionic current through the porous electrode.

2.2. Simplifications and assumptions

(1) The fuel cell is operated at steady state;

(2) The operating temperature is fixed at 60 ^oC;

(3) The convective flow in the porous layers is ignored, while the concentrations of the species at the FF/DL interfaces are regarded as the same as the feeding concentrations;

(4) The effect of the fuel crossover on the fuel cell performance is ignored, because i) the electric field across the membrane hinders the transfer of anions from the anode to cathode; ii) catalysts widely used in the cathode are inactive to the FOR, e.g., FeCoNi/C;

(5) The Donnan potential at the interface between the AEM and electrolyte is neglectable, since the induced voltage is relatively low, as the OH^- concentrations in the electrolyte and the membrane are comparable;

(6) The specific active surface area in the CLs is constant and independent of the porosity.

2.3. Governing equations and boundary conditions

2.3.1. Transport of reactants/products

The transport of the species in liquid phase is described by the diffusion-migration model, where the flux of species N_i is given as [39]

$$N_i = -D_i^{eff}\frac{dc_i}{dx} + z_i u_i^{eff} c_i F\overrightarrow{E_l} \quad (3)$$

where D_i^{eff}, c_i, z_i, u_i^{eff} and x are the effective diffusivity, local concentration, charge number and effective mobility of the species i, respectively, while x, F and $\overrightarrow{E_l}$ are the coordinate in through-plane direction, Faraday's constant and the electric field strength in the electrolyte, respectively.

The effective diffusivity D_i^{eff} is influenced by the porosity of the porous layers, which is given as [33]:

$$D_i^{eff} = \varepsilon^{3/2} D_i \quad (4)$$

where ε is the porosity and D_i is the diffusivity in supporting electrolyte.

The effective mobility is obtained from the Einstein relationship with the diffusivity [39]:

$$u_i^{eff} = D_i^{eff}/RT \tag{5}$$

where R and T denote the universal gas constant and the temperature.

At the FF/DL interface, the concentrations of the species are regarded to be the same as the feeding concentrations:

$$c_i^{FF/DL} = c_i^{feed} \tag{6}$$

where c_i^{feed} is the feeding concentration of the species i.

At the CDL/CCL interface, the concentrations of K^+ and OH^- ions are specified as:

$$c_{K^+}^{CDL/CCL} = c_{OH^-}^{CDL/CCL} = c_{KOH}^{CCL} \tag{7}$$

where c_{KOH}^{CCL} is the KOH concentration in the CCL.

The fluxes of the species are further governed by the mass conservation law [39]:

$$-\nabla N_i + S_i = 0 \tag{8}$$

where S_i denotes the source term of the species i.

It is known that an aqueous solution in fuel cells is basically electrically neutral, except at the electrode-electrolyte interface, where the charged ions are distributed in the electrical double layer [40]. As the thickness of the electrical double layer is even smaller than 10 nm, which is far smaller than the model dimension, the detailed ion distribution in the electrical double layer is ignored. Hence, the electroneutrality can be maintained by [39]:

$$\sum^N z_i c_i = 0 \tag{9}$$

where N is the total number of the ion types.

2.3.2. Electrochemical reactions

The local current density on the active surface in the CLs is governed by the Butler-Volmer functions [36], and the effects of the local reactant concentrations on the exchange current density are considered as well.

The local current density in the ACL is given as [33]:

$$j_a = j_a^0 \left(\frac{c_{HCOO^-}}{c_{HCOO^-}^{ref}}\right)^{\gamma_a^{HCOO^-}} \left(\frac{c_{OH^-}}{c_{OH^-}^{ref}}\right)^{\gamma_a^{OH^-}} \left(\exp\left(\frac{\alpha_{a,a} F \eta_a}{RT}\right) - \exp\left(\frac{-\alpha_{a,c} F \eta_a}{RT}\right)\right) \quad (10)$$

$$\gamma_a^{FM} = \begin{cases} 0 & c_{HCOO^-} > c_{HCOO^-}^{ref} \\ 1 & c_{HCOO^-} \leq c_{HCOO^-}^{ref} \end{cases} \quad (11)$$

$$\gamma_a^{OH^-} = \begin{cases} 0 & c_{OH^-} > c_{OH^-}^{ref} \\ 1 & c_{OH^-} \leq c_{OH^-}^{ref} \end{cases} \quad (12)$$

where the c_i^{ref} represents the reference concentration of the reactant i, j_a^0 is the anode exchange current density, $\alpha_{a,a}$ and $\alpha_{a,c}$ represent the anodic/cathodic electron transfer coefficients on the anode and η_a is the anode overpotential.

In the CCL, the local current density is given as [33]:

$$j_c = j_c^0 \left(\frac{c_{O_2}}{c_{O_2}^{ref}}\right)^{\gamma_c^{O_2}} \left(\exp\left(\frac{\alpha_{c,a} F \eta_c}{RT}\right) - \exp\left(\frac{-\alpha_{c,c} F \eta_c}{RT}\right)\right) \quad (13)$$

$$\gamma_a^{O_2} = \begin{cases} 0 & c_{O_2} > c_{O_2}^{ref} \\ 1 & c_{O_2} \leq c_{O_2}^{ref} \end{cases} \quad (14)$$

where $\alpha_{c,a}$ and $\alpha_{c,c}$ represent the anodic/cathodic electron transfer coefficient on the cathode, j_c^0 is the cathode exchange current density and η_c is the cathode overpotential.

2.3.3. Ionic conduction through AEM

As only OH^- ions are considered to transport through the AEM, the fluxes of the species in the membrane are given as [39]:

$$\begin{cases} N_i = 0 & (i \neq OH^-) \\ N_{OH^-} = -\frac{i_l}{F} \end{cases} \tag{15}$$

and boundary conditions of the fluxes are specified at AEM/CL interfaces [39]:

$$\begin{cases} N_i^{AEM/CL} = 0 & (i \neq OH^-) \\ N_{OH^-}^{AEM/CL} = -\frac{i_l}{F} \end{cases} \tag{16}$$

where i_l is the ionic current density.

2.3.4. Electronic and ionic conductions through porous electrodes

The electronic current in the porous electrode can be expressed as [39]:

$$i_s = \sigma_s^{eff}\overrightarrow{E_s} = -\frac{d\emptyset_s}{dx} \tag{17}$$

where i_s and σ_s^{eff} are the electronic current density and the effective electronic conductivity in DLs and CLs, while $\overrightarrow{E_s}$ and $\emptyset_s$ are the electric field strength and electric potential in porous electrodes.

The effective electronic conductivity of the porous electrode is calculated as [41]:

$$\sigma_s^{eff} = (1-\varepsilon)^{3/2}\sigma_s \tag{18}$$

where σ_s is the electronic conductivity in electrode materials.

The electrochemical reactions taking place in the ACL and CCL result in the consumptions of reactants and the productions of products:

$$\text{ACL: } S_i = R_i = \frac{n_{a,i}}{n_a F} j_a \rho_{A_{ACL}} \tag{19}$$

$$\text{CCL: } S_i = R_i = \frac{n_{c,i}}{n_c F} j_c \rho_{A_{CCL}} \tag{20}$$

where $n_{a,i}$ and $n_{c,i}$ are the participating electron numbers of the species i in the anode and cathode, n_a and n_c are the numbers of the anode and cathode transferred electrons, j_a and j_c are the local current densities in the anode and cathode, $\rho_{A_{ACL}}$ and $\rho_{A_{CCL}}$ are the specific active surface area of the ACL and CCL, while R_i denotes the consumption/production rate of the species i.

The electrode potential is determined by the theoretical equilibrium potential (E_a^0 and E_c^0) and the overpotential (η_a and η_c) as follows [39]:

$$\text{ACL: } E_a = E_a^0 + \eta_a \tag{21}$$

$$\text{CCL: } E_c = E_c^0 + \eta_c \tag{22}$$

where E_a^0 and E_c^0 are the theoretical anode and cathode potentials, respectively.

In the porous electrode saturated with liquid electrolyte, the electrolyte potential in the CLs is calculated based on the definition of the electrode potential [39]:

$$\text{Electrode potential: } E = \emptyset_l - \emptyset_s \tag{23}$$

$$\text{Electrolyte potential in the ACL: } \emptyset_{a,l} = \emptyset_{a,s} + E_a \tag{24}$$

$$\text{Electrolyte potential in the CCL: } \emptyset_{c,l} = \emptyset_{c,s} + E_c \tag{25}$$

where $\emptyset_l$ and $\emptyset_s$ are the electrolyte potential and electric potential, respectively.

The conservation of charge can be expressed as [39]:

$$\text{Charge conservation in the ACL: } \nabla \cdot i_s = -\nabla \cdot i_l = \rho_{A_{ACL}} j_a \tag{26}$$

$$\text{Charge conservation in the CCL: } \nabla \cdot i_s = -\nabla \cdot i_l = \rho_{A_{CCL}} j_c \tag{27}$$

The total ionic current in the electrolyte can be expressed as [39]:

$$i_l = \sum^N F z_i N_i \tag{28}$$

At two AEM/CL interfaces, the electrolyte potential is simplified to be continuous, where the Donnan potential is ignored [42]:

$$\emptyset_{m,l}^{AEM/ACL} = \emptyset_{a,l} \tag{29}$$

$$\emptyset_{m,l}^{AEM/CCL} = \emptyset_{c,l} \tag{30}$$

The electrolyte potential drop (overpotential) through the AEM is given as [39]:

$$\Delta\emptyset_{m,s} = \frac{\delta_m}{\sigma_m} i_l \tag{31}$$

where δ_m and σ_m are the thickness and the ionic conductivity of the AEM, respectively.

At the ADL/AFF interface, the electronic current density and electric potential are given as [39]:

$$i_s^{AFF/ADL} = i \tag{32}$$

$$\emptyset_{a,s}^{AFF/ADL} = 0 \tag{33}$$

where i is the fuel cell current density.

As various aforementioned governing equations are followed, charge conservation is maintained, and the electronic current density released from the cathode will be equal to the given current density i [39]:

$$i_s^{\mathrm{CFF/CDL}} = \mathrm{i} \tag{34}$$

Meanwhile, according to the definition of the cell voltage, the electric potential at the CDL/CFF interface represents the cell voltage [39]:

$$\mathrm{V_{cell}} = \emptyset_{\mathrm{c,s}}^{\mathrm{CFF/CDL}} - \emptyset_{\mathrm{c,s}}^{\mathrm{AFF/CDL}} = \emptyset_{\mathrm{c,s}}^{\mathrm{CFF/CDL}} - 0 = \emptyset_{\mathrm{c,s}}^{\mathrm{CFF/CDL}} \tag{35}$$

3. Validations, comparisons, and limitations

The physicochemical parameters, mass and charge transport properties, operating conditions and structural design parameters are given in Tables 1-4. The modeling results are compared with the experimental data published by Bartrom et al. [18], as shown in Figure 2(a). The comparison shows that the modeling results well fit the experimental data.

Figure 2(b) shows a comparison among three models: Model #1 (the present model that incorporates the ion migration and considers the anode catalyst layer thickness), Model #2 (the model that considers the anode catalyst layer thickness but does not consider the ion migration) and Model #3 (the model that simplifies the anode catalyst layer as an interface and does not consider the ion migration [33]. It can be seen that Model #2 predicts higher current densities than Model #1 does. This is because when the ion migration is considered, the reactants, i.e., OH^- and $HCOO^-$ ions, are dragged by K^+ ions and thus the transport is slowed down. Since the reactant concentration is overestimated, the concentration loss is

lowered and thus the fuel cell voltage is higher. As Model #3 treats the anode catalyst layer thickness as an interface, the reactant concentration loss in the anode catalyst layer is not considered, resulting in a higher voltage. In summary, incorporating both migration and diffusion in mass/charge transport and considering the anode catalyst layer thickness can provide more information, such as local concentration, and thus predict more accurate fuel cell performance.

In Figure 2(c), the voltage loss of the DFFC is divided into three parts, i.e., anode loss, cathode loss and membrane loss. It can be seen that even at the low current density (50 mA cm^{-2}), the two electrode losses are very large, since the slow reaction kinetics at a low temperature (60 ^{o}C) cause a large activation loss. With increasing the current density to 200 mA cm^{-2}, the increment of the anode loss is small. When the current density is increased to 300 mA cm^{-2}, it can be seen that the increment of the anode loss becomes large, which is attributed to the fact that the high consumption rate leads to insufficient local concentration of $HCOO^{-}$ ions in the ACL. The increment of the anode loss makes the fuel cell reach the limiting current density at 342 mA cm^{-2}. On the other hand, it can be seen that the membrane loss is much smaller than the anode and the cathode losses, since the overpotentials of two electrodes are relatively high.

In Figure 3, the distribution the electrode potential (vs. SHE) at various current densities are depicted. It can be seen that: i) the anode potential increases while the cathode potential decreases with the current density, due to the increase in the local current density and the decrease in local concentrations of reactants; ii) the increase of two electrode overpotentials with the current density turns to be slow in the medium current density range, while the

anode overpotential increases fast again in the high current density range, because the local concentrations of reactants become insufficient.

4. Results and discussion

4.1. Effects of operating conditions

4.1.1. The feeding concentration of HCOOK

Figure 4(a) shows the polarization curves of the AEM DFFC when it is operated under various feeding concentrations of HCOOK (0.5, 1.0, 1.5 and 2.0 M) and 2.0 M KOH. With the increase in the HCOOK concentration, the maximum current density increases significantly. The maximum current density under 2.0 M-HCOOK operation is around 340 mA cm^{-2}, while the maximum current density decreases to around ~78 mA cm^{-2} with 0.5 M HCOOK. Furthermore, it can be seen that the voltage decreases with the increase in current density significantly around the maximum current density. The variation trends of the fuel cell performance can be explained by the concentration distributions of $HCOO^-$ ions in the anode, as shown in Figure S1(a). It can be seen that the $HCOO^-$ concentration in the ACL decreases very fast with the increase in the current density. In the high current density range, the local concentration of $HCOO^-$ becomes insufficient. On the other hand, the OH^- distribution is not changed with the change of the HCOOK feeding concentration, as shown in Figure S1(b). The anode performance is limited by the insufficient local $HCOO^-$ concentration at high current density. When the HCOOK feeding concentration is increased, the local $HCOO^-$ concentration in the ACL is effectively increased and thus the maximum current density is promoted. In summary, the HCOOK feeding concentration shows significant influence on the fuel cell performance, because the local $HCOO^-$

concentration in the ACL is the bottleneck of the anode performance and the HCOOK feeding concentration affects the local $HCOO^-$ concentration significantly.

4.1.2. The feeding concentration of KOH

Figure 4(b) shows the polarization curves of the AEM DFFC when it is operated under various feeding concentrations of KOH (0.5, 1.0, 1.5 and 2.0 M) and 2.0 M HCOOK. The maximum current density under 2.0 M-HCOOK operation is around 345 mA cm^{-2}. With the decrease in the KOH feeding concentration from 2.0 M to 1.5 M and 1.0 M, the maximum current density is decreased slightly to 340 and 330 mA cm^{-2}. When the KOH feeding concentration is further decreased, the decrease in the maximum current density is accelerated to about 295 mA cm^{-2}. The results can be explained by the concentration distributions of OH^- and $HCOO^-$ ions in the anode, as shown in Figures S2(a) and (b). It can be seen that the concentration of OH^- ions in the ACL is decreased slowly with the increase in the current density, because the diffusivity and mobility of OH^- ions are high, and more importantly, OH^- ions in the ACL are additionally supplied from the adjacent AEM. Therefore, the $HCOO^-$ ions in the ACL firstly become insufficient in the high current density range. When the KOH feeding concentration is in the range of 1.0~2.0 M, the OH^- concentration in the ACL is relatively high, resulting in the similar concentration loss. When the KOH feeding concentration is as low as 0.5 M, the OH^- concentration in the ACL is low and the anode overpotential is consequently large, lowering the fuel cell performance. In summary, the influence of the KOH feeding concentration is not significant, because the OH^- concentration in the ACL is almost sufficient due to the additional supply from the cathode.

4.2. Effects of anode structural parameters

4.2.1. The thickness of the anode diffusion layer

Figure 5(a) shows the polarization curves of the DFFC under various ADL thicknesses (50, 100, 150 and 200 μm). The cell voltage is reduced significantly with the increase in the ADL thickness, and the maximum current density is also decreased from 700 mA cm^{-2} to 175 mA cm^{-2} with the increase in the ADL thickness. From the concentration distributions of $HCOO^-$ and OH^- ions, which are shown in Figures S3(a) and (b), it can be found that the concentrations of $HCOO^-$ and OH^- ions in the ACL gradually decrease with the increase of the ADL thickness due to the increased transport distance of reactants, degrading the fuel cell performance. In summary, the thinner ADL will improve the fuel cell performance because the transport distance of the reactants is reduced and thus the local concentration of reactants in the ACL is increased. However, it shall be mentioned that when a flow field is applied in a DFFC, an ADL with an appropriate thickness is helpful to the reactant delivery to the under-rib area.

4.2.2. The porosity of the anode diffusion layer

Figure 5(b) shows the polarization curves of the DFFC under various ADL porosities (0.6, 0.7, 0.8 and 0.9). The fuel cell performance upgrades with the increase in the ADL porosity. From the concentration distributions of $HCOO^-$ and OH^- ions, as shown in Figures S4(a) and (b), it can be seen that the increase of the ADL porosity largely increases the reactant concentrations in the ACL due to the smaller mass transport resistance, upgrading the fuel cell performance. In summary, higher porosity of the ADL will reduce the mass transport resistance and thus improve the fuel cell performance. However, it shall be noted that too high porosity of the ADL will result in a low mechanical stability of the electrode and reduce the substrate to support the catalyst particles, which shall be avoided.

4.2.3. The thickness of the anode catalyst layer

Figure 5(c) shows the polarization curves of the DFFC under various ACL thicknesses (10, 25, 50 and 100 μm). It can be seen that the increase in the ACL thickness increases the cell voltage in the current density range of 0~260 mA cm^{-2}. This can be explained by the local current density distributions and the anode overpotential distributions, as shown in Figures S5(a) and (b). When the current density is low, the lower local current density and lower overpotential are obtained when the ACL is thicker, because larger active surface area is provided. When the current density is high, the FOR occurs intensively in the small region adjacent to the ADL, while in the remaining region of the ACL the active surface area is not used due to the absence of reactants. Therefore, the higher thickness of the ACL has no contribution to the fuel cell performance in the high current density range. While in the high current density region, it can be seen that the cell voltage decreases with the increase in the thickness of the ACL, which is due to the fact that the transport distance of the OH^- ions from the AEM becomes larger, slightly enlarging the ohmic loss. In summary, a thicker ACL enlarges the active surface area and thus reduces the local current density in the low current density range, while in the high current density range the cell voltage will be reduced because of increasing the ohmic loss.

4.2.4. The porosity of the anode catalyst layer

Figure 5(d) shows the polarization curves of the DFFC under various ACL porosities (0.2, 0.4, 0.6 and 0.8), and the local current density distributions and the anode overpotential distributions are shown in Figures S6(a) and(b). It can be seen that the increase in the ACL porosity increases the cell voltage significantly in the high current density range but shows no influence in the low current density range. This is explained by the following reasons:

i) when the current density is low, the reactant consumption is small, and thus the whole ACL possesses sufficient reactants; ii) when the current density is high, the mass transport resistance of the ACL leads to the considerable concentration loss in the ACL; iii) a higher porosity increases the accessibility of the active surface being accessible for the reactants and thus the local current density is distributed more uniform; and iv) the uniform distribution lowers the local current density and thus decreases the anode overpotential. In summary, a higher ACL porosity reduces mass transport resistance in the ACL, leading to more active surface accessible to reactants, and thus it improves the fuel cell performance, especially in the high current density range.

4.3. Effects of cathode structural parameters

4.3.1. The thickness of the cathode catalyst layer

Figure 6 shows the polarization curves of the DFFC under various CCL thicknesses (10, 25, 50 and 100 μm). It can be seen that an increase in the CCL thickness increases the cell voltage in almost the whole current density range. This can be explained by the cathode local current density distributions and the cathode overpotential distributions, as shown in Figures S7(a) and (b). It can be seen that the cathode local current density distributed uniformly in the whole current density range due to the superior transport property of oxygen in the CCL. The higher the CCL thickness is, the more active surface area is provided and thus the local current density is lowered. The decrease in the local current density further results in the lower cathode overpotential and thus the cell voltage is increased. Compared to the anode, the decrease in the cell voltage with the increase in the CCL thickness does not occur since the gas transport is much more efficient and thus the reactant can access all the active surface even at high current densities. In summary,

increasing the CCL thickness increases the fuel cell performance because the increased active surface area reduces the local current density and thus reduces the cathode overpotential.

4.4. Effects of specific active surface area

4.4.1. The anode specific active surface area

Figure 7(a) shows the polarization curves of the DFFC under different anode specific active surface area (1.6×10^{8}, 1.6×10^{9}, 1.6×10^{10} and 1.6×10^{11} m^{-1}), and the local current density distributions and anode overpotential distributions are shown in Figures S8(a) and (b). It can be seen that, with increasing the specific active surface area to ten times, the fuel cell voltage increases by 0.077 V in all the current density range. The reason can be found in Figures S8(a) and (b). With the increase in the specific active surface area to ten times, the local current density is reduced greatly to one tenth, as indicate by the Figure S8(a). Furthermore, it can be derived from the governing equation of the electrochemical reaction kinetics in the ACL that, with the decrease in the local current density to one tenth, the anode overpotential will be reduced by $2.3\frac{RT}{\alpha_{a,a}}$. The derivation is given as follows [33]:

$$j_a = j_a^0\left(\frac{c_{HCOO^-}}{c_{HCOO^-}^{ref}}\right)^{\gamma_a^{HCOO^-}}\left(\frac{c_{OH^-}}{c_{OH^-}^{ref}}\right)^{\gamma_a^{OH^-}}\left(\exp\left(\frac{\alpha_{a,a}F\eta_a}{RT}\right)-\exp\left(\frac{-\alpha_{a,c}F\eta_a}{RT}\right)\right)$$

$$\approx j_a^0\left(\frac{c_{HCOO^-}}{c_{HCOO^-}^{ref}}\right)^{\gamma_a^{HCOO^-}}\left(\frac{c_{OH^-}}{c_{OH^-}^{ref}}\right)^{\gamma_a^{OH^-}}\exp\left(\frac{\alpha_{a,a}F\eta_a}{RT}\right) \quad (35)$$

$$\frac{1}{10}j_a = j_a^0\left(\frac{c_{HCOO^-}}{c_{HCOO^-}^{ref}}\right)^{\gamma_a^{HCOO^-}}\left(\frac{c_{OH^-}}{c_{OH^-}^{ref}}\right)^{\gamma_a^{OH^-}}\left(\exp\left(\frac{\alpha_{a,a}F\eta'_a}{RT}\right)-\exp\left(\frac{-\alpha_{a,c}F\eta'_a}{RT}\right)\right)$$

$$\approx j_a^0\left(\frac{c_{HCOO^-}}{c_{HCOO^-}^{ref}}\right)^{\gamma_a^{HCOO^-}}\left(\frac{c_{OH^-}}{c_{OH^-}^{ref}}\right)^{\gamma_a^{OH^-}}\exp\left(\frac{\alpha_{a,a}F\eta'_a}{RT}\right) \quad (36)$$

$$\eta'_{a} - \eta_{a} = \ln\left(\frac{1}{10}\right)\frac{RT}{\alpha_{a,a}} \approx -2.3\frac{RT}{\alpha_{a,a}} \approx -0.077 \text{ V} \quad (37)$$

The decrease in the anode overpotential is also evidenced by the Figure S4(c). Thereby, it can be concluded that, with the increase in the specific active surface area of the ACL, the fuel cell performance is improved, because the local current density is reduced and thus the anode overpotential is lowered.

4.4.2. The cathode specific active surface area

Figure 7(b) shows the polarization curves of the DFFC under different cathode specific active surface area (1.6×10^8, 1.6×10^9, 1.6×10^{10} and 1.6×10^{11} m^{-1}), and the local current density distributions and cathode overpotential distributions are shown in Figures S9(a) and (b). It can be seen that, with increasing the specific active surface area, the fuel cell voltage increases in all the current density range. From Figures S9(a) and (b), it can be seen that the reason of the performance improvement is the decreases in the local current density and the cathode overpotential. With the increase in the specific active surface area of the CCL to ten times, the cathode overpotential will be reduced by $2.3\frac{RT}{\alpha_{c,c}}$, according to the theoretical derivation. As the three-phase cathodic electron transfer is more sluggish than the anodic electron transfer ($\alpha_{c,c} = 0.5 < \alpha_{a,a} = 0.85$), the influence of the specific active surface area of the CCL on the fuel cell performance is more significant. With the increase in the specific active surface area of the CCL to ten times, the reduction of the cathode overpotential reaches 0.13 V. Therefore, when the specific active surface area is as low as 1.6×10^8 m^{-1}, the cathode reaction kinetics becomes the bottleneck of the fuel cell performance.

5. Concluding remarks

In this work, a one-dimensional mathematical model for anion exchange membrane direct formate fuel cells incorporating the effect of ion migration is developed. The model involves the diffusion and migration of the reactants as well as the electrochemical reactions: i) the transport of various species, i.e., K^+, $HCOO^-$, OH^-, CO_3^{2-} and O_2, ii) the electrochemical reactions on the active surface, iii) the ionic current conduction through the membrane, iv) the electronic and ionic current conduction through the porous electrode.. The incorporated ion migration brings two advantageous characteristics compared to the conventional diffusion-predominated transport model: i) the prediction of the concentration distributions of the reactants/products can be more accurate, and ii) the local current density distribution in the CLs can be revealed. In the validation, the model results exhibit a good agreement with the experimental data [18]. The voltage losses resulting from the anode, membrane and cathode, as well as the distribution of the electrode potential are specified. The effects of the operating conditions, i.e., the feeding concentrations of reactants in the fuel solution, and the structural design parameters, i.e., the thicknesses, porosities and specific active surface area of the diffusion layers and the catalyst layers, on the fuel cell performance are examined. The main findings are summarized as follows: i) the cell voltage drop is mainly attributed to the anode and cathode overpotentials; ii) the maximum current density of the fuel cell is limited by the transport of formate ions, and increasing the feeding concentration of formate will increase the maximum current density via increasing the local formate-ion concentration; iii) the feeding concentration of alkali shows relatively neglectable influence on the anode performance, because the hydroxide-ion concentration is almost sufficient even when the feeding concentration is low and the consumption rate is high, as a result of the fact that the anode catalyst layer additionally

receives the hydroxide ions that come from the cathode; iv) both decreasing the thickness and increasing the porosity of the anode diffusion layer will increase the fuel cell voltage and the maximum current density, as a result of the decreased mass transport resistance of the reactants; v) in the low current density range, increasing the thickness of the anode catalyst layer will reduce the anode overpotential, since the overall active surface area is enlarged and thus the distributed local current density is decreased; while it leads to very neglectable decrease in the fuel cell voltage at high current densities, because the ionic pathway is extended; vi) increasing the porosity of the anode catalyst layer leads to a lower concentration loss since the mass transport resistance of reactants is reduced; vii) increasing the thickness of the cathode catalyst layer enlarges the active surface area and thus decreases the cathode overpotential; and viii) increasing the specific active surface area of the anode/cathode catalyst layer leads the anode/cathode overpotential to decrease significantly, because the local current density is reduced and thus the electrode overpotential is decreased.

Acknowledgements

This work was fully supported by a grant from the Research Grants Council of the Hong Kong Special Administrative Region, China (Project No. 25211817).

References

[1] L. An, R. Chen, Direct formate fuel cells: A review, Journal of Power Sources 320 (2016) 127-139.

[2] D. K. Ross, Hydrogen storage: The major technological barrier to the development of hydrogen fuel cell cars, Vacuum 80 (2006) 1084-1089.

[3] D. Mori, K. Hirose. Recent challenges of hydrogen storage technologies for fuel cell vehicles, International Journal of Hydrogen Energy 34 (2009) 4569-4574.

[4] M. Felderhoff, C. Weidenthaler, R. V. Helmolt, U. Eberle. Hydrogen storage: the remaining scientific and technological challenges, Physical Chemistry Chemical Physics 9 (2007) 2643-2653.

[5] L. An, T. S. Zhao, R. Chen, Q. X. Wu, A novel direct ethanol fuel cell with high power density, Journal of Power Sources 196 (2011) 6219-6222.

[6] L. An, T. S. Zhao, S. Y. Shen, Q. X. Wu, R. Chen, Performance of a direct ethylene glycol fuel cell with an anion-exchange membrane, International Journal of Hydrogen Energy 35 (2010) 4329-4335.

[7] L. An, T. S. Zhao, S. Y. Shen, Q. X. Wu, R. Chen, Alkaline direct oxidation fuel cell with non-platinum catalysts capable of converting glucose to electricity at high power output, Journal of Power Sources 196 (2011) 186-190.

[8] Y. S. Li, T. S. Zhao, Ultra-low catalyst loading cathode electrode for anion-exchange membrane fuel cells, International Journal of Hydrogen Energy 37 (2012) 15334-15338.

[9] Y. S. Li, T. S. Zhao, A passive anion-exchange membrane direct ethanol fuel cell stack and its applications, International Journal of Hydrogen Energy 4 (2016) 20336-20342.

[10] Y. S. Li, T. S. Zhao, Z. X. Liang, Performance of alkaline electrolyte-membrane-based direct ethanol fuel cells, Journal of Power Sources 187 (2009) 387-392.

[11] Y. S. Li, T. S. Zhao, J. B. Xu, S. Y. Shen, W. W. Yang, Effect of cathode micro-porous layer on performance of anion-exchange membrane direct ethanol fuel cells, Journal of Power Sources 196 (2011) 1802-1807.

[12] Q. X. Wu, L. An, X. H. Yan, T. S. Zhao, Effects of design parameters on the performance of passive direct methanol fuel cells fed with concentrated fuel, Electrochimica Acta 133 (2014) 8-15.

[13] Q. X. Wu, T. S. Zhao, R. Chen, L. An, A sandwich structured membrane for direct methanol fuel cells operating with neat methanol, Applied Energy 106 (2013) 301-306.

[14] Y. S. Li, T. S. Zhao, A high-performance integrated electrode for anion-exchange membrane direct ethanol fuel cells, International Journal of Hydrogen Energy 36 (2011) 7707-7713.

[15] A. K. Shukla, C. L. Jackson, K. Scott, R. K. Raman, An improved-performance liquid-feed solid-polymer-electrolyte direct methanol fuel cell operating at near-ambient conditions, Electrochimica Acta 47 (2002) 3401-3407.

[16] Y. S. Li, A liquid-electrolyte-free anion-exchange membrane direct formate-peroxide fuel cell, International Journal of Hydrogen Energy 41 (2016) 3600-3604.

[17] T. Vo, K. Purohit, C. Nguyen, B. Biggs, S. Mayoral, J.L. Haan, Formate: An energy storage and transport bridge between carbon dioxide and a formate fuel cell in a single device, ChemSusChem 8 (2015) 3853-3858.

[18] A. M. Bartrom, J. L Haan, The direct formate fuel cell with an alkaline anion exchange membrane, Journal of Power Sources 214 (2012) 68-74.

[19] A. M. Bartrom, J. Ta, T. Q. Nguyen, J. Her, A. Donovan, J. L. Haan, Optimization of an anode fabrication method for the alkaline direct formate fuel cell, Journal of Power Sources 229 (2013) 234-238.

[20] T. Q. Nguyen, D. Minami, C. Hua, A. Miller, K. Tran, J. L. Haan, Ambient temperature operation of a platinum-free direct formate fuel cell, Journal of Fuel Cell Science and Technology 12 (2015) 014501.

[21] J. Jiang, A. Wieckowski, Prospective direct formate fuel cell, Electrochemistry Communications 18 (2012) 41-43.

[22] L. Q. Wang, M. Bellini, J. Filippi, M. Folliero, A. Lavacchi, M. Innocenti, A. Marchionni, H.A. Miller, Vizza, F, Energy efficiency of platinum-free alkaline direct formate fuel cells, Applied Energy 175 (2016) 479-487.

[23] H. Miller, J. Ruggeri, A. Marchionni, M. Bellini, M. Pagliaro, C. Bartoli, A. Pucci, E. Passaglia, F. Vizza, Improving the energy efficiency of direct formate fuel cells with a Pd/C-CeO_2 anode catalyst and anion exchange ionomer in the catalyst layer, Energies 11 (2018) 369.

[24] T. Q. Nguyen, A. M. Bartrom, K. Tran, J. L. Haan, Operation of the alkaline direct formate fuel cell in the absence of added hydroxide, Fuel Cells 13 (2013) 922-926.

[25] X. Sun, Y. Li, Understanding mass and charge transports to create anion-ionomer-free high-performance alkaline direct formate fuel cells, International Journal of Hydrogen Energy 44 (2019) 7538-7543.

[26] X.Y. Su, Z.F. Pan, L. An, Performance characteristics of a passive direct formate fuel cell, International Journal of Energy Research 43 (2019) 7433-7443.

[27] X.Y. Su, Z.F. Pan, L. An, Three-dimensional porous electrodes for direct formate fuel cells, SCIENCE CHINA Technological Sciences (2020) in press.

[28] Y.S. Li, Y. Feng, X.D. Sun, Y.L. He. A sodium‐ion‐conducting direct formate fuel cell: generating electricity and producing base, Angewandte Chemie International Edition 56 (2017) 5734-5737.

[29] K. Jiao, S. Huo, M. Zu, D. Jiao, J. Chen, Q. Du, An analytical model for hydrogen alkaline anion exchange membrane fuel cell, International Journal of Hydrogen Energy 40 (2015) 3300-3312.

[30] H. Deng, J. Chen, K. Jiao, X. Huang, An analytical model for alkaline membrane direct methanol fuel cell, International Journal of Heat and Mass Transfer 74 (2014) 376-390.

[31] S. Heysiattalab, M. Shakeri, 2D analytical model for direct ethanol fuel cell performance prediction, Smart Grid and Renewable Energy 2 (2011) 427.

[32] Z. Pan, Y. Bi, L. An, Mathematical modeling of direct ethylene glycol fuel cells incorporating the effect of the competitive adsorption, Applied Thermal Engineering 147 (2019) 1115-1124.

[33] L. An, R. Chen, Mathematical modeling of direct formate fuel cells, Applied Thermal Engineering 124 (2017) 232-240.

[34] X.Y. Su, Z.F. Pan, L. An, Ion transport characteristics in membranes for direct formate fuel cells, Frontiers in Chemistry 8 (2020) 765.

[35] Y. L. He, Z. Miao, T. S. Zhao, W. W. Yang, Numerical study of the effect of the GDL structure on water crossover in a direct methanol fuel cell, International Journal of Hydrogen Energy 37 (2012) 4422-4438.

[36] D. A. Stevens, J. R. Dahn, Electrochemical characterization of the active surface in carbon-supported platinum electrocatalysts for PEM fuel cells, Journal of The Electrochemical Society 150 (2003) A770-A775.

[37] L. An, T. S. Zhao, Q. X. Wu, L. Zeng, Comparison of different types of membrane in alkaline direct ethanol fuel cells, International Journal of Hydrogen Energy 37 (2012) 14536-14542.

[38] N. Zamel, X. Li, J. Shen, Numerical estimation of the effective electrical conductivity in carbon paper diffusion media, Applied Energy 93 (2012) 39-44.

[39] X. L. Zhou, T.S. Zhao, L. An, Y.K. Zeng, X.H. Yan, A vanadium redox flow battery model incorporating the effect of ion concentrations on ion mobility, Applied Energy 158 (2015) 157-166.

[40] K. Oldham, J. Myland, Fundamentals of Electrochemical Science, Elsevier (2012).

[41] F. G. Cuevas, J. M. Montes, J. Cintas, P. Urban, Electrical conductivity and porosity relationship in metal foams, Journal of Porous Materials 16 (2009) 675.

Figure captions

Figure 1. Computational domain of the present model.

Figure 2. (a) Comparison between the modeling results and experimental data, (b) comparison among three modeling results and (c) specific voltage losses: anode loss, membrane loss and cathode loss.

Figure 3. Distribution of the electrode potential (vs. SHE).

Figure 4. Effect of (a) HCOOK and (b) KOH feeding concentrations.

Figure 5. Effect of (a) anode diffusion layer thickness (δ_{ADL}), anode diffusion layer porosity ($\varepsilon_{\mathrm{ADL}}$), anode catalyst layer thickness (δ_{ACL}) and anode catalyst layer porosity ($\varepsilon\delta_{\mathrm{ACL}}$).

Figure 6. Effect of cathode catalyst layer thickness (δ_{CCL}).

Figure 7. Effect of (a) anode specific active surface area ($\rho_{\mathrm{A\ ACL}}$) and cathode specific active surface area ($\rho_{\mathrm{A\ CCL}}$).

Figure S1. Effect of the HCOOK feeding concentration on (a) $HCOO^-$ concentration distributions and (b) OH^- concentration distributions.

Figure S2. Effect of the KOH feeding concentration on the distributions of (a) $HCOO^-$ concentration distributions and (b) OH^- concentration distributions.

Figure S3. Effect of the anode diffusion layer thickness (δ_{ADL}) on the distributions of (a) $HCOO^-$ concentration distributions and (b) OH^- concentration distributions.

Figure S4. Effect of the anode diffusion layer porosity ($\varepsilon_{\mathrm{ADL}}$) on the distributions of (a) $HCOO^-$ concentration distributions and (b) OH^- concentration distributions.

Figure S5. Effect of the anode catalyst layer thickness (δ_{ACL}) on (a) local current density distributions and (b) anode overpotential distributions.

Figure S6. Effect of the anode catalyst layer porosity ($\varepsilon_{\mathrm{ACL}}$) on (a) local current density distributions and (b) anode overpotential distributions.

Figure S7. Effect of the cathode catalyst layer thickness (δ_{CCL}) on (a) local current density distributions and (b) cathode overpotential distributions.

Figure S8. Effect of the anode specific active surface area ($\rho_{\mathrm{A\ ACL}}$) on (a) local current density distributions and (b) anode overpotential distributions.

Figure S9. Effect of the cathode specific active surface area ($\rho_{\mathrm{A\ CCL}}$) on (a) local current density distributions and (b) cathode overpotential distributions.

Table captions

Table 1. Physicochemical parameters.

Table 2. Mass and charge transport properties.

Table 3. Operating conditions.

Table 4. Structural design parameters.

Table 1.

Physicochemical parameters.

Parameter	Symbol	Value	Unit	Re
Theoretical anode potential	E_a^0	-1.05	V	
Theoretical cathode potential	E_c^0	0.4	V	
Anodic transfer coefficient of anode	$\alpha_{a,a}$	0.85	-	
Cathodic transfer coefficient of anode	$\alpha_{a,c}$	0		
Anodic transfer coefficient of cathode	$\alpha_{c,a}$	0		
Cathodic transfer coefficient of cathode	$\alpha_{c,c}$	0.5	-	
Anode exchange current density	j_a^0	1.5×10^{-7}	A m^{-2}	
Cathode exchange current density	j_c^0	6.6×10^{-7}	A m^{-2}	
Universal gas constant	R	8.3145	J $(mol\ K)^{-1}$	
Faraday's constant	F	96485	C mol^{-1}	
Number of anode transferred electrons	n_a	2	-	
Number of cathode transferred electrons	n_c	4	-	

Table 2.

Mass and charge transport properties.

Parameter*	Symbol	Value	Unit	Reference
Diffusivity of K^+	D_{K^+}	1.96×10^{-9}	$m^2\ s^{-1}$	[33]
Diffusivity of OH^-	D_{OH^-}	5.27×10^{-9}	$m^2\ s^{-1}$	[33]
Diffusivity of CO_3^{2-}	$D_{CO_3{}^{2-}}$	0.92×10^{-9}	$m^2\ s^{-1}$	[33]
Diffusivity of $HCOO^-$	D_{HCOO^-}	1.45×10^{-9}	$m^2\ s^{-1}$	[33]
Diffusivity of O_2	D_{O_2}	2.55×10^{-5}	$m^2\ s^{-1}$	[33]

Table 3.

Operating conditions.

Parameter	Symbol	Value	Unit	Re
Operating temperature	T	333	K	
Gas pressure	P	1.01×10^5	Pa	
Feeding concentration of $HCOO^-$	$c_{HCOO^-}^{feed}$	2.0	M	
Feeding concentration of OH^-	$c_{OH^-}^{feed}$	2.0	M	
Feeding concentration of CO_3^{2-}	$c_{CO_3^{2-}}^{feedt}$	0	M	
Feeding concentration of O_2	$c_{O_2}^{feed}$	P/RT	M	
Reference concentration of $HCOO^-$	$c_{HCOO^-}^{ref}$	2.0	M	
Reference concentration of OH^-	$c_{OH^-}^{ref}$	2.0	M	
Reference concentration of O_2	$c_{O_2}^{ref}$	P/RT	M	
KOH concentration for the CCL	c_{KOH}^{CCL}	1.0	M	As

Table 4.

Structural design parameters.

Parameter	Symbol	Value	Unit
Thickness of anode diffusion layer	δ_{ADL}	1.0×10^{-4}	m
Porosity of the anode diffusion layer	ε_{ADL}	0.75	-
Thickness of anode catalyst layer	δ_{ACL}	0.5×10^{-4}	m
Porosity of the anode catalyst layer	ε_{ACL}	0.4	-
Anode specific active surface	$\rho_{A_{ACL}}$	1.6×10^{10}	m^{-1}
Thickness of anion exchange membrane	δ_M	2.8×10^{-5}	m
Ionic conductivity of anion exchange membrane	σ_M	2.5	Ω^{-1} m
Thickness of cathode catalyst layer	δ_{CCL}	0.5×10^{-4}	m
Porosity of the cathode CL	ε_{CCL}	0.4	-
Cathode specific active surface	$\rho_{A_{CCL}}$	1.6×10^{10}	m^{-1}
Thickness of cathode diffusional layer	δ_{CDL}	1.0×10^{-4}	m
Porosity of the cathode diffusional layer	ε_{CDL}	0.75	-
Electronic conductivity of the electrode solid material (ε=0)	σ_s	1.2×10^{4}	Ω^{-1} m

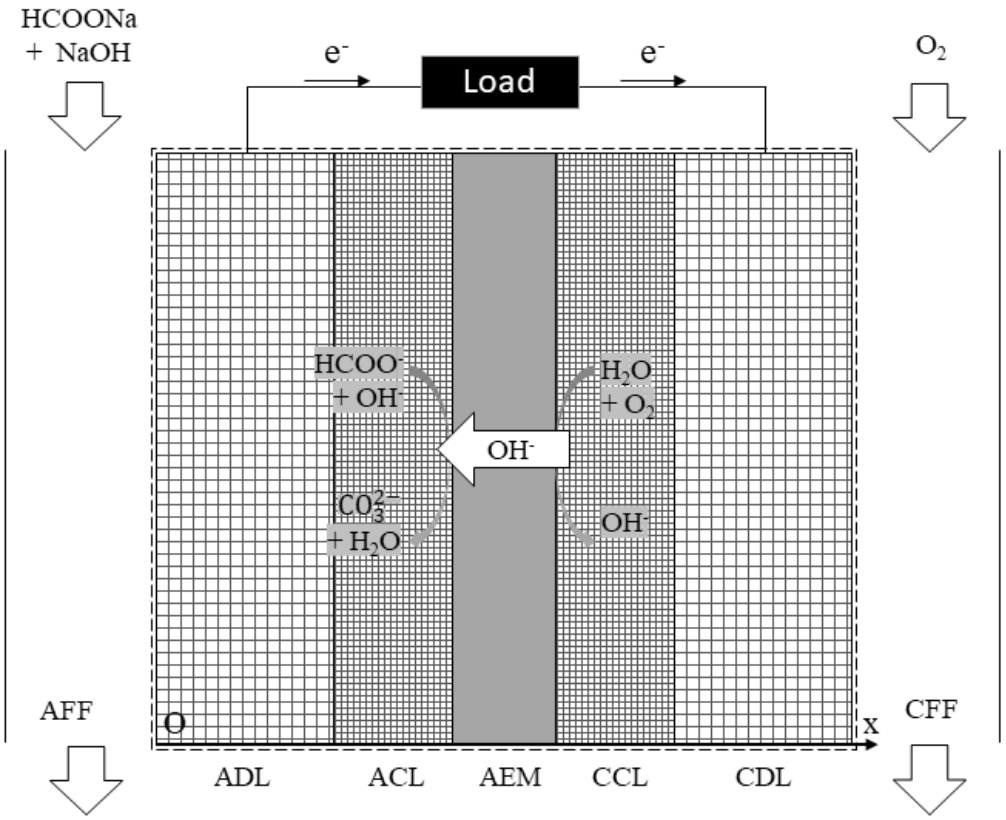

Figure 1. Computational domain of the present model.

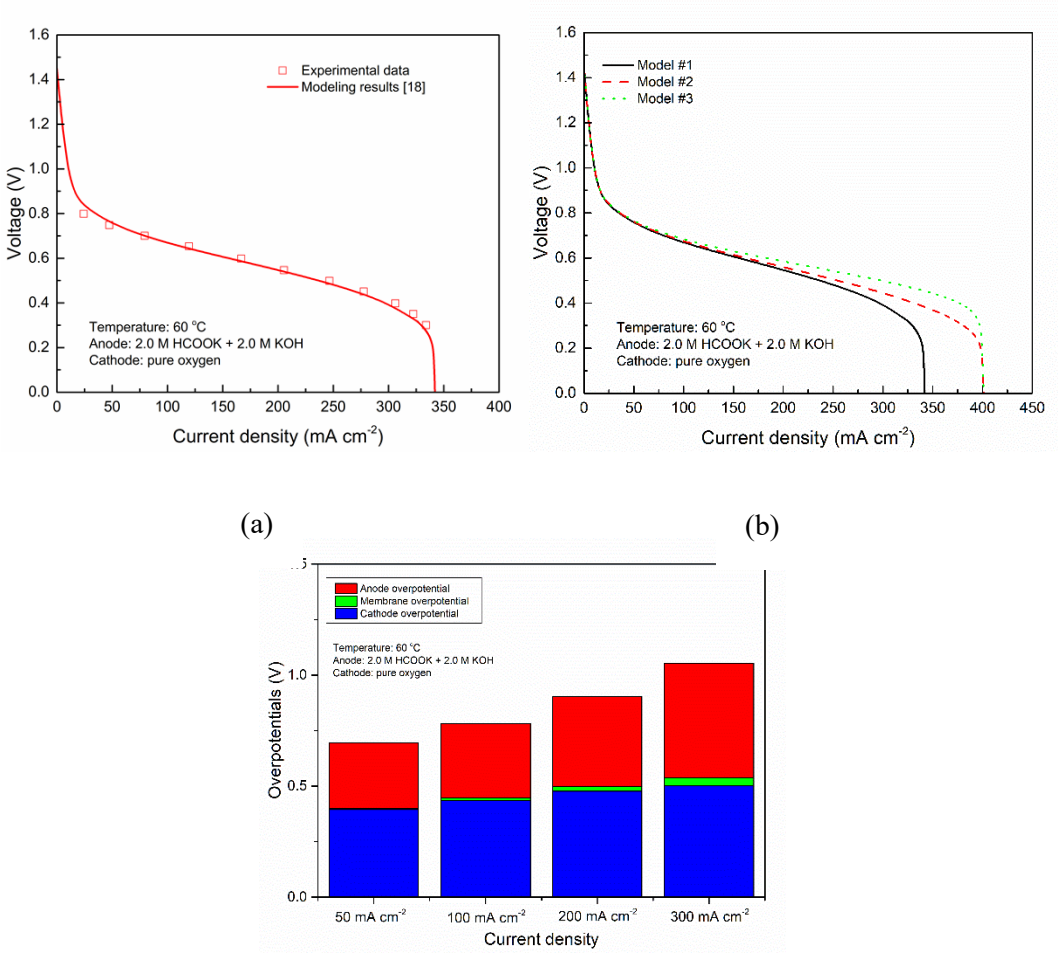

Figure 2. (a) Comparison between the modeling results and experimental data, (b) comparison among three modeling results and (c) specific voltage losses: anode loss, membrane loss and cathode loss.

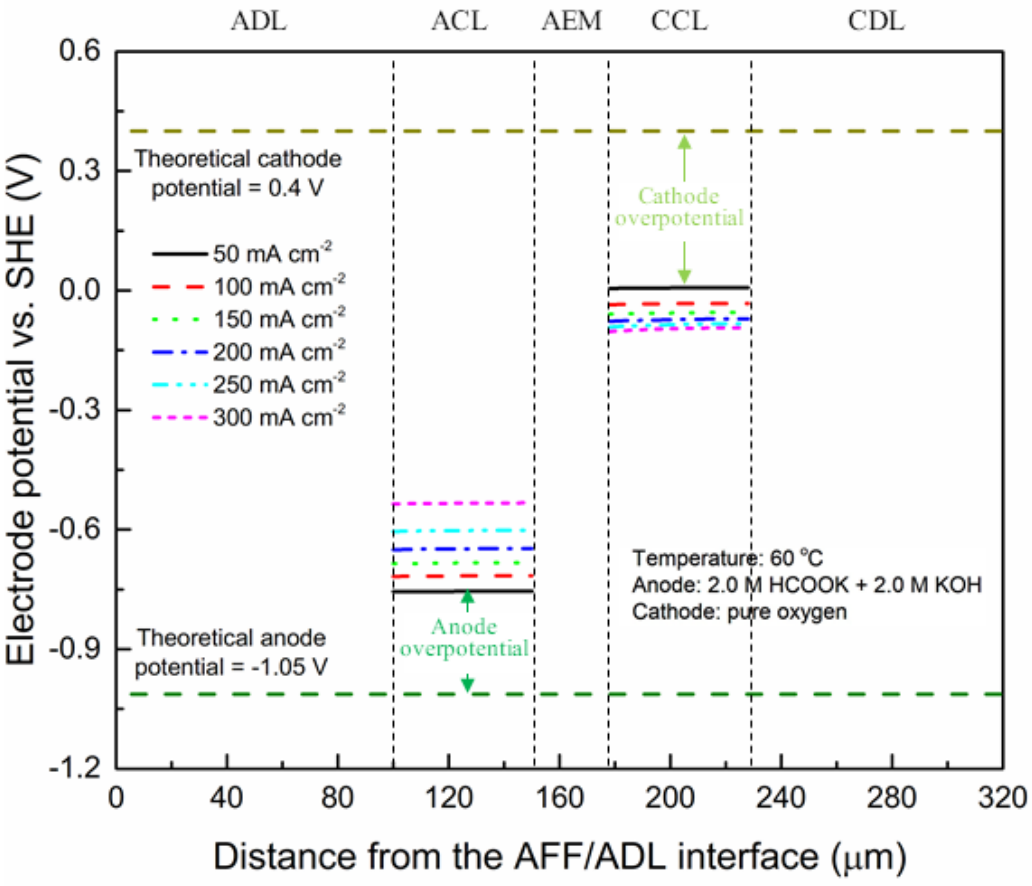

Figure 3. Distribution of the electrode potential (vs. SHE).

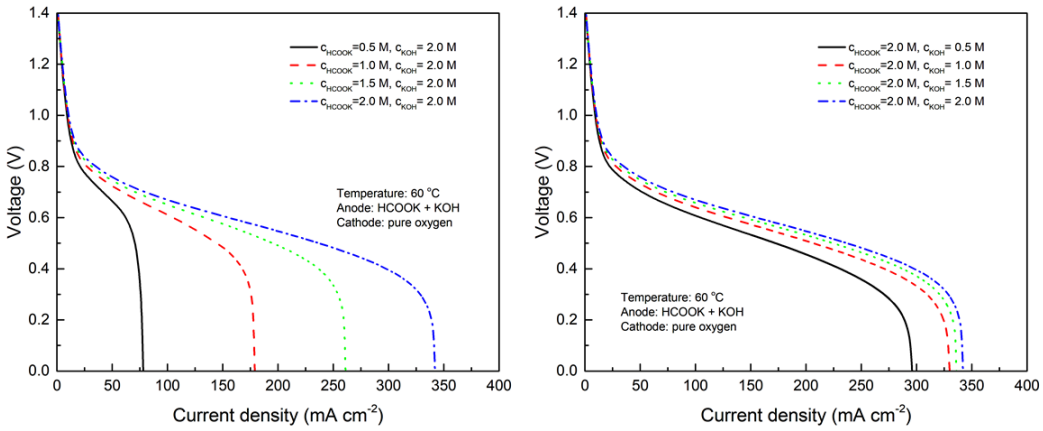

Figure 4. Effect of (a) HCOOK and (b) KOH feeding concentrations.
(a) (b)

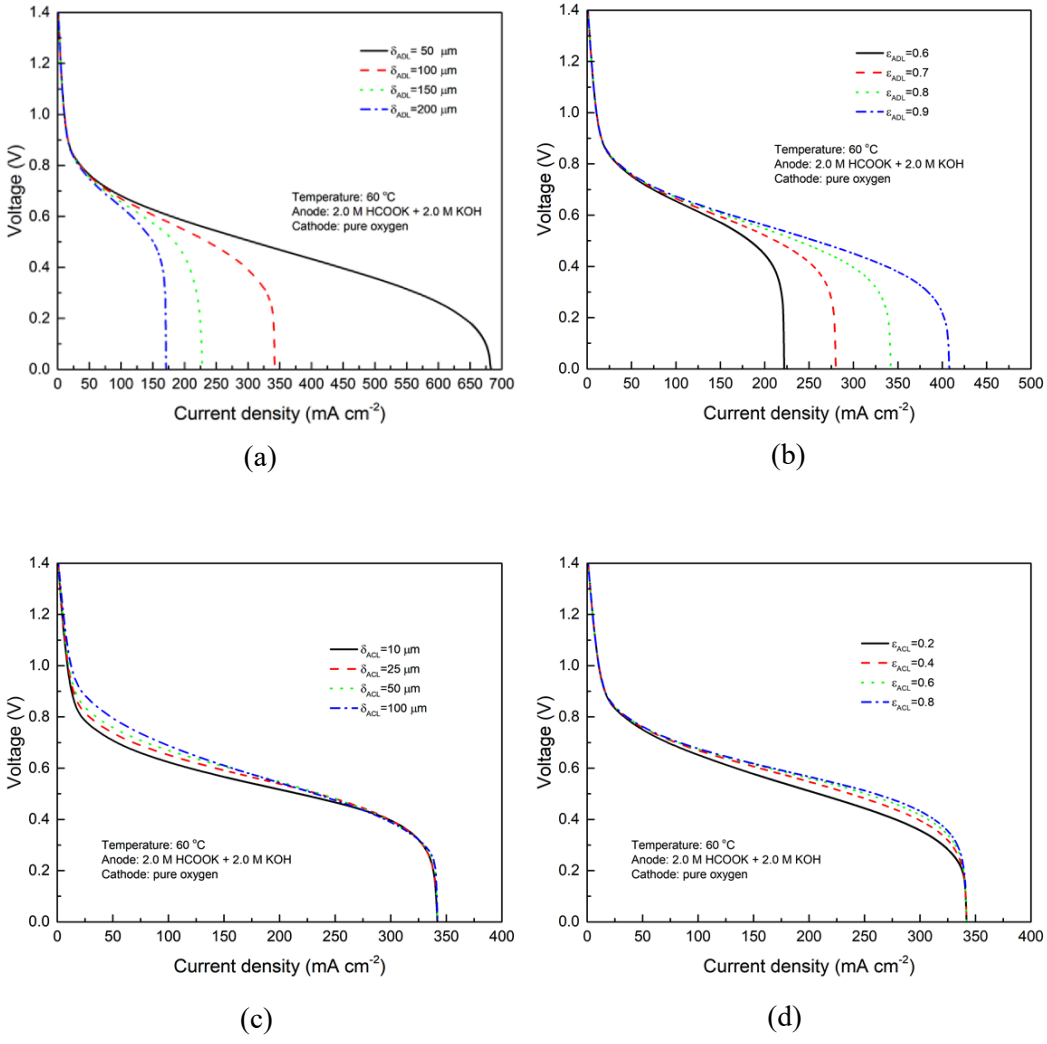

Figure 5. Effect of (a) anode diffusion layer thickness (δ_{ADL}), anode diffusion layer porosity (ε_{ADL}), anode catalyst layer thickness (δ_{ACL}) and anode catalyst layer porosity ($\varepsilon\delta_{ACL}$).

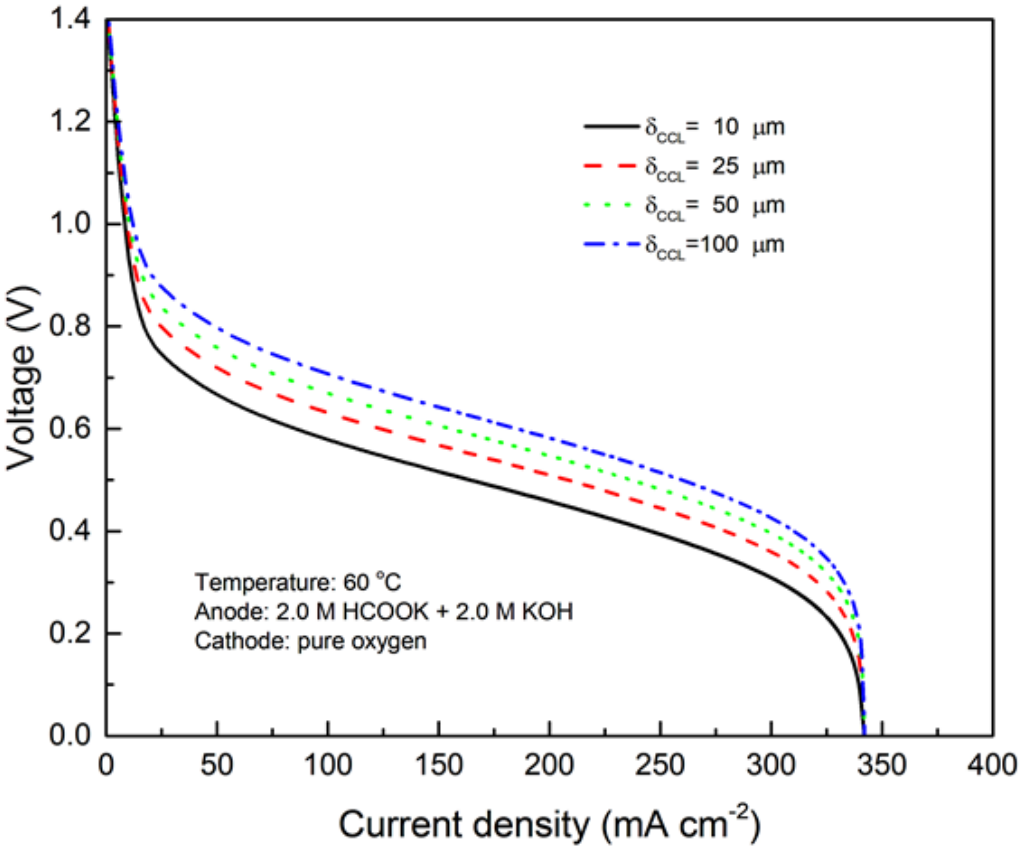

Figure 6. Effect of cathode catalyst layer thickness (δ_{CCL}).

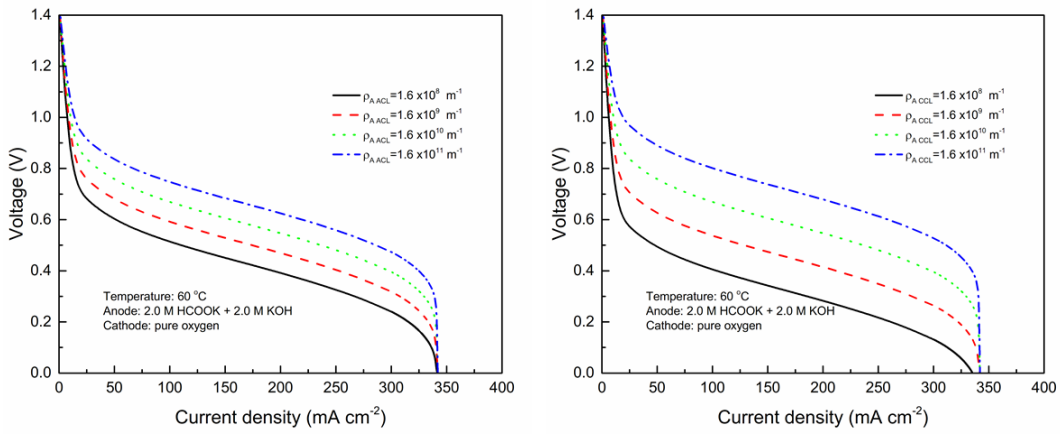

(a) (b)

Figure 7. Effect of (a) anode specific active surface area ($\rho_{A\ ACL}$) and cathode specific active surface area ($\rho_{A\ CCL}$).